



Phase-dependent Evolution within the Large Luminosity Range of 1A 0535+262 Observed by Insight-HXMT during 2020 Giant Outburst

Ling-Da Kong^{1,2} , Shu Zhang¹, Long Ji³, Victor Doroshenko^{4,5} , Andrea Santangelo⁴ , Mauro Orlandini⁶ , Filippo Frontera⁷ , Jian Li⁸ , Yu-Peng Chen¹, Peng-Ju Wang^{1,2} , Zhi Chang¹ , Jin-Lu Qu¹, and Shuang-Nan Zhang^{1,2}

¹ Key Laboratory for Particle Astrophysics, Institute of High Energy Physics, Chinese Academy of Sciences, 19B Yuquan Road, Beijing 100049, People's Republic of China; kongld@ihep.ac.cn, szhang@ihep.ac.cn

² University of Chinese Academy of Sciences, Chinese Academy of Sciences, Beijing 100049, People's Republic of China

³ School of Physics and Astronomy, Sun Yat-Sen University, Zhuhai, 519082, People's Republic of China; jilong@mail.sysu.edu.cn

⁴ Institut für Astronomie und Astrophysik, Kepler Center for Astro and Particle Physics, Eberhard Karls, Universität, Sand 1, D-72076 Tübingen, Germany

⁵ Space Research Institute of the Russian Academy of Sciences, Profsoyuznaya Str. 84/32, Moscow 117997, Russia

⁶ INAF/Osservatorio di Astrofisica e Scienza dello Spazio, Via Gobetti 101, I-40129 Bologna, Italy

⁷ Department of Physics and Earth Science, University of Ferrara, Via Saragat, 1 I-44122 Ferrara, Italy

⁸ CAS Key Laboratory for Research in Galaxies and Cosmology, Department of Astronomy, University of Science and Technology of China, Hefei 230026, People's Republic of China

Received 2022 January 29; revised 2022 May 7; accepted 2022 May 9; published 2022 June 21

Abstract

We have performed phase-resolved spectral analysis of the accreting pulsar 1A 0535+262 based on observations of Insight-HXMT during the 2020 type II outburst of the source. We focus on the two-dimensional dependence of the cyclotron resonance scattering features (CRSFs) along the outburst time and at different phases. The fundamental CRSF line (f-CRSF) shows different time- and phase-dependent behaviors. At higher luminosity, the phase profile of the f-CRSF energy changes from a single peak to double peaks, with the transition occurring at MJD 59185. On the contrary, the first harmonic CRSF (first CRSF) at ~ 100 keV is only detected within a narrow phase range (0.8–1.0) accompanied by a shallow f-CRSF line. Based on these results, we speculate that when the source enters the supercritical regime, the higher accretion column height can significantly enhance the harmonic line at a narrow phase through an “anti-pencil” beam at a higher energy band. At the same time, it will also affect the behavior of the fundamental line.

Unified Astronomy Thesaurus concepts: Binary pulsars (153); High mass x-ray binary stars (733); Accretion (14); Magnetic fields (994)

1. Introduction

1A 0535+262 is a transient high-mass X-ray binary (HMXB) located 2 kpc away (Bailer-Jones et al. 2018) with a highly magnetized neutron star (NS) spinning ~ 104 s and orbiting an O9.7IIIe donor star (Rosenberg et al. 1975; Steele et al. 1998). The orbit has an eccentricity of $e = 0.47 \pm 0.02$ and an orbital period of $P_{\text{orb}} \sim 110.3 \pm 0.3$ days (Finger et al. 1996).

The magnetic field strength $\sim 4 \times 10^{12}$ G of 1A 0535+262 was measured through the discovery of a fundamental cyclotron resonance scattering feature (CRSF) at ~ 45 keV (Kendziorra et al. 1994). The CRSF energy is related to the magnetic field strength of the NS surface by the “12-B-12 rule,” $E_{\text{cyc}} \approx 12B_{12}$ keV, with the B -field strength B_{12} given in units of 10^{12} G (Canuto & Ventura 1977).

A cyclotron line at energy higher than 90 keV was first predicted by dal Fiume et al. (1988), who observed the source with a balloon experiment during the 1980 giant outburst, from the comparison between the observed spectrum and the theoretical spectra expected for different values of the magnetic field by Harding et al. (1984). The presence of a first harmonic line at 110 keV was later observed with Compton Gamma Ray Observatory (CGRO) OSSE during an outburst in 1994, but the 45 keV feature was not detected (Grove et al. 1995). During the 2005 type I outburst of the source, two absorption features were

detected in the phase-averaged spectra at ~ 45 and ~ 100 keV (Caballero et al. 2007), based on INTEGRAL observations. Caballero et al. (2008) also detected a CRSF at ~ 50 keV with slightly higher energy during a pre-outburst flare about five days prior to the normal outburst. The authors suggested that this was related to a short accretion episode triggered by magnetospheric instabilities (Postnov et al. 2008).

The evolution of the CRSF's parameters with luminosity provides essential information for studying accreting flow geometry and physics near the NS surface (Maitra 2017). Caballero et al. (2007) considered all CRSF measurements for 1A 0535+262 using data from RXTE, INTEGRAL, Suzaku, and TTM & HEXE and found no correlation between the CRSF parameters and luminosity, therefore suggesting that the line-forming region does not significantly vary with luminosity. Positive E_{cyc}/L_x correlation was found using “pulse-to-pulse” analysis (Klochkov et al. 2011). At the higher luminosities, Sartore et al. (2015) suggested that 1A 0535+26 accretes in the subcritical regime, and they found no significant variations of the energy of its cyclotron lines with flux by phase-average spectral analysis. During the brightest 2020 type II outburst, Kong et al. (2021), based on Insight-HXMT data, found a clear transition between positive and negative correlation at a critical luminosity 6.7×10^{37} erg s $^{-1}$, showing that the source changed the accretion regime from subcritical to supercritical (Basko & Sunyaev 1976; Becker et al. 2012; Mushtukov et al. 2015). Below the critical luminosity, 1A 0535+262 showed an asymmetrical evolution during the outburst, and the CRSF energy remained stable during the decreasing phase, implying



Original content from this work may be used under the terms of the [Creative Commons Attribution 4.0 licence](https://creativecommons.org/licenses/by/4.0/). Any further distribution of this work must maintain attribution to the author(s) and the title of the work, journal citation and DOI.

the complexity again in understanding the CRSF (Kong et al. 2021). This finding made 1A 0535+262 the second source showing a transition between super- and subcritical accretion after V0332+53 (Doroshenko et al. 2017; Vybormov et al. 2018), but with an opposite trend.

Kong et al. (2021) also found that the CRSF centroid energy ratio of the first harmonic line to the fundamental line was ~ 2.3 , larger than the factor of 2 predicted from the spacing of the Landau levels. Similar results were found for Vela X-1 (Kreykenbohm et al. 2002). Such behavior can be explained by photon spawning from scattering at higher harmonics (producing lower-harmonic photons from a higher-harmonic photon). Hence, the depth and shape of the fundamental line can be influenced (Schönherr et al. 2007). However, Nishimura (2011) explained this behavior as due to a superposition of a large number of line energies that arose from different heights of the accretion column.

In this work, we present an investigation of the variation of key spectral parameters as a function of the pulse phase, obtained with the finest ever phase and time sampling in a broad energy band. Section 2 describes observations and data reduction, and our results are presented in Section 3. In Section 4, we discuss our results. The summary and conclusions are presented in Section 5.

2. Observation and Data Reduction

The Hard X-ray Modulation Telescope, named Insight-HXMT (Zhang et al. 2014; Zhang et al. 2020), was launched on 2017 June 15. The scientific payload includes three collimated telescopes that allow observations in a broad energy band (1–250 keV) and with large effective area at high energies: the High Energy X-ray Telescope (HE, 18 cylindrical NaI(Tl)/CsI(Na) phoswich detectors, Liu et al. 2020), the Medium Energy X-ray Telescope (ME, 1728 Si-PIN detectors, Cao et al. 2020), and the Low Energy X-ray Telescope (LE, Swept Charge Device (SCD), Chen et al. 2020), with collecting area/energy range of $5000 \text{ cm}^2/20\text{--}250 \text{ keV}$, $952 \text{ cm}^2/5\text{--}30 \text{ keV}$, and $384 \text{ cm}^2/1\text{--}10 \text{ keV}$. The fields of view (FOVs) are $1^\circ 6' \times 6^\circ$, $1^\circ \times 4^\circ$, and $1^\circ 1' \times 5^\circ 7'$ and $5^\circ 7' \times 5^\circ 7'$ for LE, ME, and HE, respectively, with two FOVs for HE (narrow FOV for 15 detection units, large FOV for 2 units, 1 unit with blocked FOV; see Figure 1 in Kong et al. 2021).

Insight-HXMT observed 1A 0535+262 from 2020 November 6 (MJD 59159) to 2020 December 24 (MJD 59207), for a total exposure of ~ 1.910 Ms. In Figures 1 and 2, observation at the peak of the outburst on 2020 November 18 (MJD 59171) with a long exposure time (LE: 12.14 ks; ME: 12.11 ks; HE: 13.96 ks) is shown as a demonstration of phase-resolved analysis in 10 phases (~ 1 ks exposure time for each detector), which can show high signal-to-noise ratio (S/N) of the spectrum above 100 keV and constrain the CRSF energy well. For all observations, the phase-resolved spectral analysis shown in Figure 3 investigates the spectral components throughout the outburst well. For the analysis, we use the Insight-HXMT Data Analysis Software (HXMTDAS) v2.04, together with the current calibration model v2.05 (<http://hxmtweb.ihep.ac.cn/software.jhtml>). The data are selected as recommended by the Insight-HXMT team. In particular, data with elevation angle (ELV) larger than 10° , geometric cutoff rigidity (COR) larger than 8 GeV, and offset for the point position smaller than $0^\circ 04'$ are used. In addition, data taken within 300 s of the South Atlantic Anomaly (SAA) passage

outside of good time intervals identified by onboard software have been rejected. Contamination from Crab (R.A. = 83.63308, decl. = 22.0145) has been taken into account as in Kong et al. (2021).

Based on the results of in-flight calibration (Li et al. 2020), the energy bands considered for spectral analysis are 1.5–10 keV for the LE, 8–35 keV for the ME, and 28–120 keV for the HE. Because of the uncertain calibration of the Ag emission line at ~ 22 keV of the ME, we ignore the 20–23 keV range during the spectral analysis for this instrument. The instrumental backgrounds are estimated with the tools provided by the Insight-HXMT team: LEBKGMAP, MEBKGMAP, and HEBKGMAP, version 2.0.9 based on the standard Insight-HXMT background models (Liao et al. 2020a, 2020b; Guo et al. 2020). The XSPEC v12.12.0 software package (Arnaud 1996) was used to perform the spectral fitting. To improve the counting statistic of the energy spectra, we combined the exposures within 1 day by *addspec* and *addrmf* tasks. Considering the current accuracy of the instrument calibration, we include 0.5%, 0.5%, and 1% systematic error for spectral analysis for LE, ME, and HE, respectively. The uncertainties of the spectral parameters are computed using Markov Chain Monte Carlo (MCMC) with a length of 10,000 and are reported at a 90% confidence level.

3. Results

3.1. Pulse Profiles and Phase-resolved Spectra

In the following timing analysis, barycentric and binary orbiting corrections have been performed for period determination and studying of pulse profiles, and the parameters of the binary orbit ($T_0 = 53,613$, $P_{\text{orbit}} = 111.1$ days, $e = 0.47$, $ax \sin i = 267$ lt-s, $\omega = 130^\circ$) are taken from Finger et al. (1996). Because of high statistics, the HE observations are used to measure periods in each interval. To ensure that the phases from different observations are consistent, all HE pulse profiles (25–80 keV) with two peaks are aligned to get times of arrival (TOAs) through the FFTFIT routine (Taylor 1992). We use tempo2 to fit the TOA evolution (Hobbs et al. 2006) and get the frequency parameters.⁹

The background-subtracted light curves of LE, ME, and HE are folded with 12 energy bands: 1.5–3 keV, 3–5 keV, 5–8 keV, 10–15 keV, 15–20 keV, 20–30 keV, 30–50 keV, 50–70 keV, 70–90 keV, 90–110 keV, 110–150 keV, and 150–200 keV. The pulse profiles are normalized by average counting rate. Taking an observation (2020 November 18) during the peak of the outburst, where the luminosity exceeded the critical one, as an example, the pulse profiles (left panels of Figure 1) show clear energy dependence: multiple peaks at lower energies (< 10 keV) and double peaks at higher energies (> 20 keV). And we find that the peaks of pulse profiles simplify at higher energy bands, and a significant dip arises at phases 0.8–1.0 at 90–110 keV, accompanied by a significant harmonic line at ~ 100 keV. As the energy increases, the profiles change from peak to valley at phases 0.8–1.0, and the phase separation between the two peaks above 20 keV gradually increases. The behaviors of the pulse profiles' evolution with energy might be related to different relativistic

⁹ $\text{pepoch} = 59170$; $F0 = 0.0096595755935471$, $F1 = 1.72126260544263e-11$, $F2 = 1.11786863370198e-17$, $F3 = -5.51116187149374e-23$, $F4 = .06922105290258e-28$, $F5 = -1.27856062979819e-34$, $F6 = 7.33508948203979e-41$ for TOA fitting.

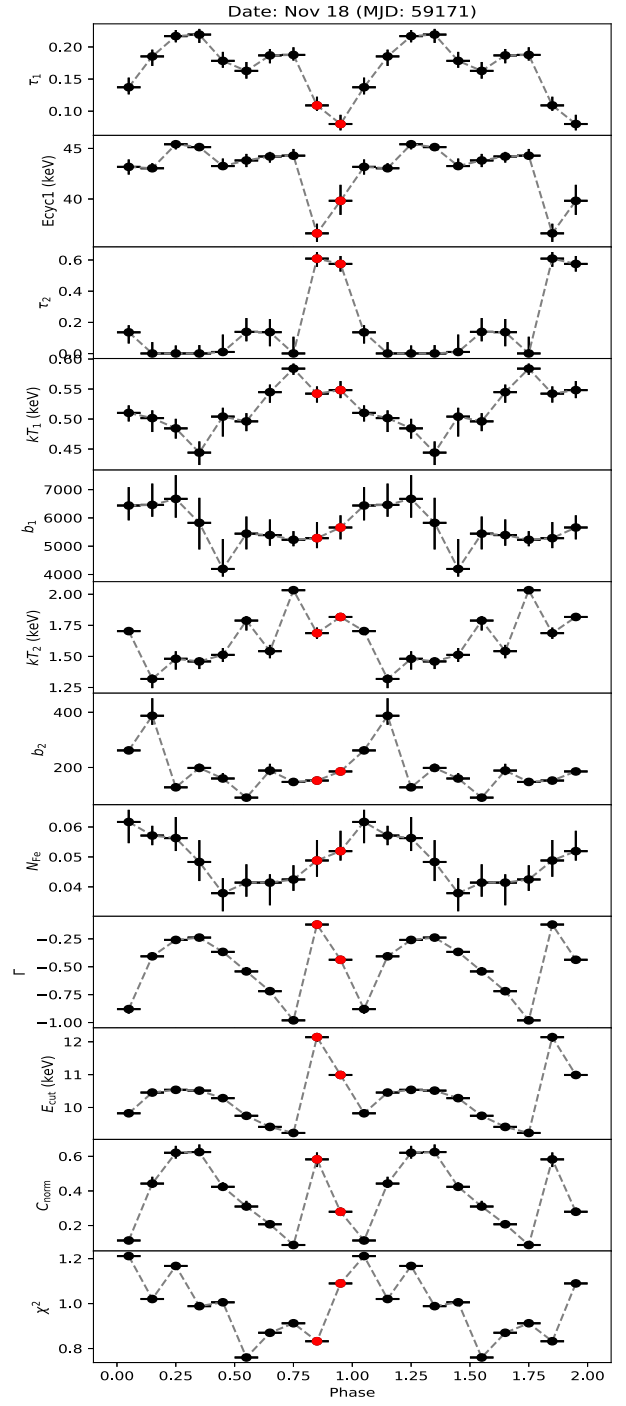
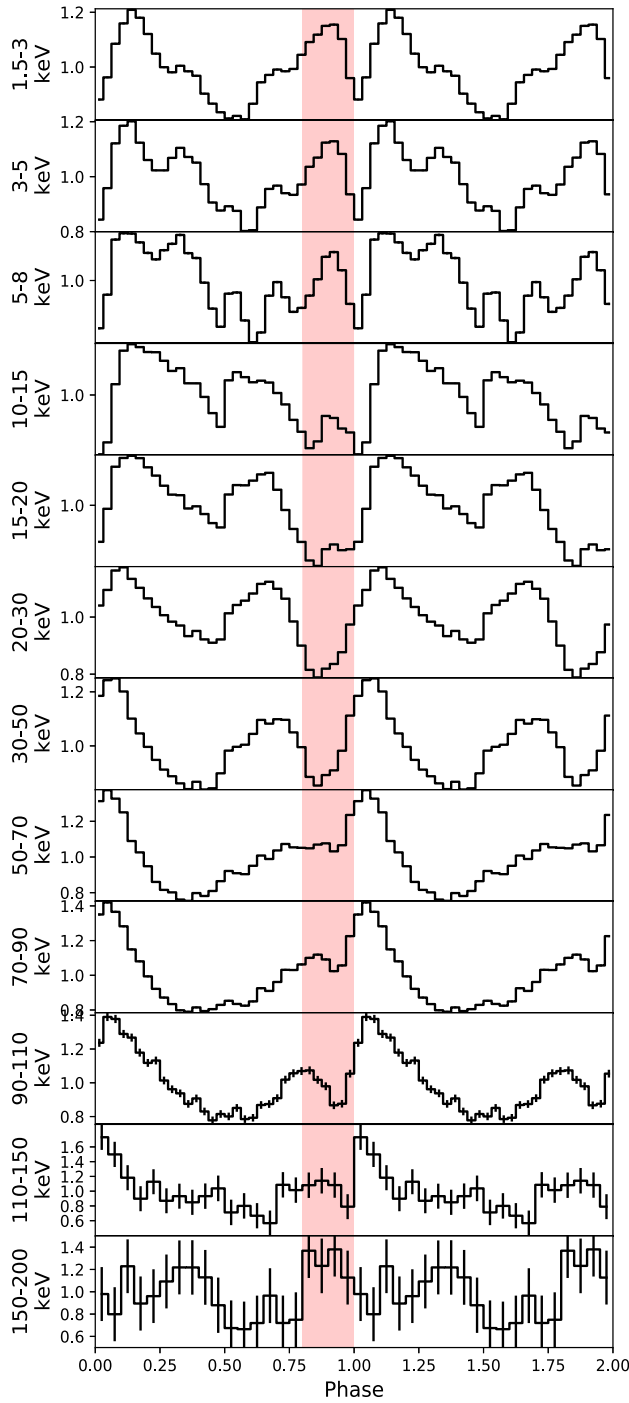


Figure 1. Left panel: the pulse profiles on MJD 59171 in different energy bands. Right panel: the phase-dependent parameters from phase-resolved spectral fittings on MJD 59171. The red points mark the phases with weak fundamental lines and strong first harmonic lines, and the phase range between 0.8 and 1.0 is filled with red color in the left panel.

beaming angles at various energy bands and will be discussed in Section 4.

In Figure 1 (right panel), Figure 2, and Table 1, we show the observation on 2020 November 18 (combine ObsID P0304099007, P0314316002, P0314316003 within 1 day) as an example. For each observation, we select the photons within 10 different phases, and the spectra are extracted from these decadal phase intervals. We use the same model $Tbabs \times mgabs \times (bbodyrad1 + bbodyrad2 + cutoffpl + Gaussian)$ in Kong et al. (2021) to fit these spectra at different phases. The

cutoffpl is a simple continuum with just three free parameters:

$$F(E) = K \times E^{-\Gamma} \exp(-E/E_{\text{fold}}), \quad (1)$$

where K , Γ , and E_{fold} determine the normalization coefficient, the photon index, and the exponential folding energy, respectively. The residuals at lower energies are accounted for by adding two blackbody components: a cooler one with $kT < 1$ keV (*bbodyrad1*), and a hotter one with $kT > 1$ keV (*bbodyrad2*). The interstellar medium absorption is taken into

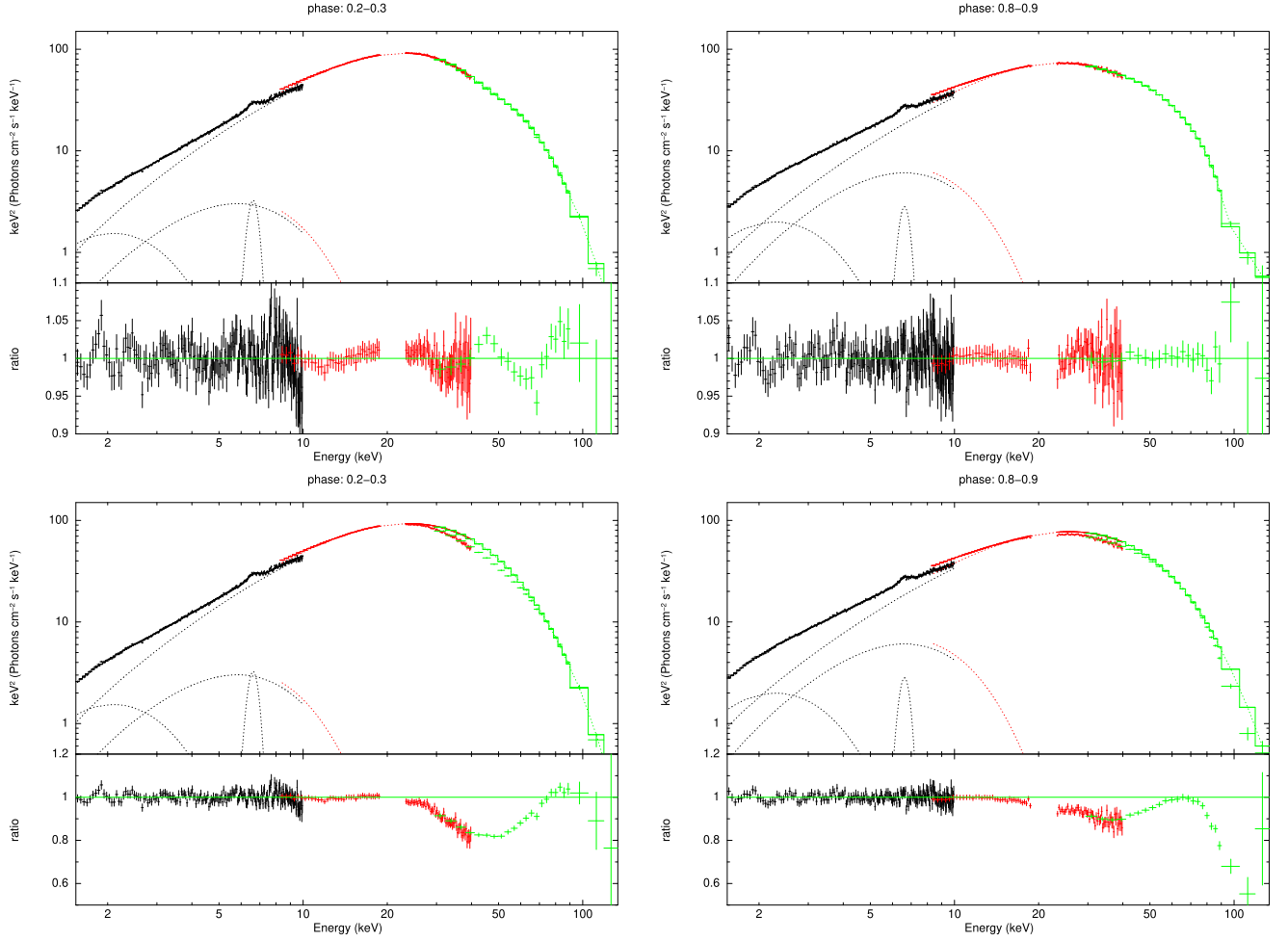


Figure 2. The spectral fittings and residuals for phase 0.2–0.3 (left) and 0.8–0.9 (right) on MJD 59171. The lower panels of the two phases show the spectral fittings and residuals without the CRSF lines.

account through the *tbabs* model (Wilms et al. 2000), where n_H is fixed at 0.59×10^{22} atoms cm^{-2} . A Gaussian line is needed to model the iron emission line, and we fix the energy at 6.6 keV and the width at 0.3 keV. To model the CRSF absorption features at ~ 45 and ~ 100 keV that are visible in the phase-average spectra in Kong et al. (2021), we adopt a “1-gabs” multiplicative absorption model *mgabs* with two Gaussian profiles (Staubert et al. 2019):

$$F'(E) = F(E) \times mgabs = F(E) \times [(1 - \tau_1 e^{-\frac{(E-E_{\text{cyc1}})^2}{2\sigma_1^2}}) \times (1 - \tau_2 e^{-\frac{(E-E_{\text{cyc2}})^2}{2\sigma_2^2}})], \quad (2)$$

where $F'(E)$ is the spectrum modified by the multiplicative model *mgabs* with “1-gabs” form, E_{cyc1} is the cyclotron line central energy of the fundamental line, and τ_1 and σ_1 characterize the central absorption depth and the width of the line, respectively. As for the fundamental line, E_{cyc2} , τ_2 , and σ_2 describe the central energy, the depth, and the width of the first harmonic line. For *mgabs*, we first set all parameters free and list the fitting results in Table 2. We also use two *gabs* to replace *mgabs*, and we list the fitting results in Table 3. From Tables 2 and 3, there are no significant differences between these two ways. The width of the fundamental line σ_1 remains relatively stable around 10–13 keV but with an extensive error

range, and the width of the harmonic line σ_2 cannot be constrained well; hence, it causes considerable uncertainty to the absorption depth τ_2 . Because the width of the fundamental CRSF remains relatively stable along with the outburst in a wide luminosity range (Sartore et al. 2015; Kong et al. 2021), we then follow the same operation and fix it at a canonical value ~ 10 keV. Here we also consider that the width will also affect the depth of the CRSF and other continuum parameters, which may make the later results and analysis need to consider more complex factors, so we only focus on the energy and depth of the CRSF. The energy and width of the first harmonic line are fixed at 100 and 10 keV based on the fitting results in phase interval 0.8–1.0, showing significant absorption structure during the spectral fitting. This also avoids the low statistic and uncertainty caused by the higher background above 100 keV. We note that the width of the 100 keV line was fixed at 5 keV in Kong et al. (2021), but for phase-resolved spectra at phases 0.8–1.0, it causes larger χ^2 and residuals. The reported uncertainties for the best-fit parameters are estimated using the MCMC method with a chain length of 10,000. The parameters and reduced χ^2 are plotted in the right panel of Figure 1 and listed in Table 1. From the spectral fitting, for the fundamental line we find that the E_{cyc1} is essentially constant with a value of ~ 44 keV except for phases 0.8–0.9, where it

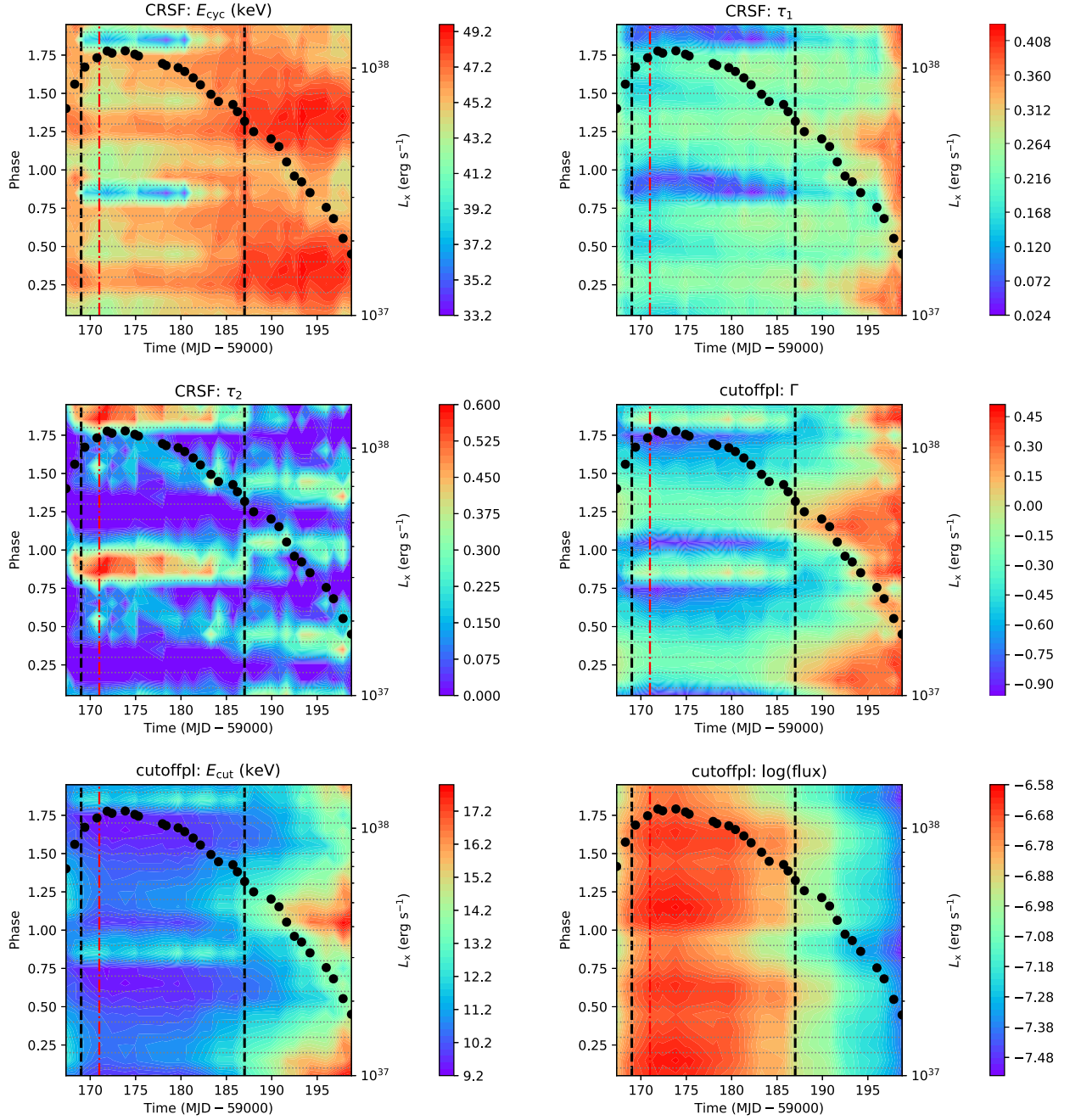


Figure 3. The 2D MJD vs. phase distributions (2D MPDs) show the CRSF energy E_{cyc} , the absorption depth τ_1 at fundamental, absorption depth at first harmonic τ_2 , photon index Γ , high-energy cut E_{cut} , and $\log(\text{flux})$ of the *cutoffpl* component in 2–150 keV. Two black dashed lines mark the time range between MJD 59169 and 59187, which is associated with the luminosity above the critical luminosity. The red dashed and dotted lines represent the MJD 59171 at the peak of the outburst. Gray dotted lines separate 10 phase intervals. The black points show how luminosities evolve with time.

drops to ~ 37 keV. The absorption depth τ_1 stays stable ~ 0.15 except at 0.8–1.0, with a dramatic drop to ~ 0.08 . The phase dependence of the depth of the fundamental line can be described as showing two peaks at pulse phases of 0.2–0.3 and 0.7–0.8 and a dip at phases 0.8–0.9. The depth, τ_2 , of the first harmonic shows a significant increase at the same phase range, whereas τ_1 exhibits a considerable decrease. Γ and E_{cut} of *cutoffpl* have abrupt increases at phases 0.8–1.0, and they show a correlated behavior versus phase. In Figure 2, we show the best fits for spectra and corresponding residuals with and without the fundamental and the first harmonic CRSF lines at phases 0.2–0.3 and 0.8–0.9, respectively.

3.2. 2D Distribution

The phase dependence and time evolution of the CRSF parameters can also be visualized using two-dimensional (2D) color maps. Such maps are shown in Figure 3 for parameters of the CRSF energy and its optical depth for the fundamental and harmonic lines, the photon index Γ , the high-energy cut E_{cut} , and the $\log(\text{flux})$ of the *cutoffpl* component in 2–150 keV. Phase dependence of all parameters exhibits an apparent change around MJD 59186.

First, the intensity and the energy E_{cyc} of the fundamental line show a single broad sinusoidal profile between MJD 59186 and 59198 during the subcritical regime, as demonstrated in the

Table 1
Parameters of the Spectral Fitting

| Phase | | 0.0 – 0.1 | 0.1 – 0.2 | 0.2 – 0.3 | 0.3 – 0.4 | 0.4 – 0.5 | 0.5 – 0.6 | 0.6 – 0.7 | 0.7 – 0.8 | 0.8 – 0.9 | 0.9 – 1.0 |
|-----------|--|---------------------------|---------------------------|---------------------------|---------------------------|---------------------------|---------------------------|---------------------------|---------------------------|---------------------------|---------------------------|
| TBabs | n_{H} (10^{22} cm^{-2}) | 0.59 (fixed) | 0.59 (fixed) | 0.59 (fixed) | 0.59 (fixed) | 0.59 (fixed) | 0.59 (fixed) | 0.59 (fixed) | 0.59 (fixed) | 0.59 (fixed) | 0.59 (fixed) |
| mgabs | E_{cyc1} (keV) | $43.2^{+0.7}_{-0.8}$ | $43.0^{+0.5}_{-0.3}$ | $45.4^{+0.4}_{-0.5}$ | $45.1^{+0.4}_{-0.4}$ | $43.3^{+0.7}_{-0.4}$ | $43.8^{+0.7}_{-0.7}$ | $44.2^{+0.5}_{-0.6}$ | $44.3^{+0.7}_{-0.3}$ | $36.6^{+1.0}_{-0.9}$ | $39.8^{+1.6}_{-1.4}$ |
| | σ_1 (keV) | 10 (fixed) | 10 (fixed) | 10 (fixed) | 10 (fixed) | 10 (fixed) | 10 (fixed) | 10 (fixed) | 10 (fixed) | 10 (fixed) | 10 (fixed) |
| | τ_1 | $0.14^{+0.01}_{-0.01}$ | $0.19^{+0.01}_{-0.01}$ | $0.22^{+0.01}_{-0.01}$ | $0.22^{+0.01}_{-0.01}$ | $0.18^{+0.01}_{-0.01}$ | $0.16^{+0.01}_{-0.01}$ | $0.19^{+0.01}_{-0.01}$ | $0.19^{+0.01}_{-0.01}$ | $0.11^{+0.01}_{-0.01}$ | $0.08^{+0.01}_{-0.01}$ |
| | E_{cyc2} (keV) | 100 (fixed) | 100 (fixed) | 100 (fixed) | 100 (fixed) | 100 (fixed) | 100 (fixed) | 100 (fixed) | 100 (fixed) | 100 (fixed) | 100 (fixed) |
| | σ_2 (keV) | 10 (fixed) | 10 (fixed) | 10 (fixed) | 10 (fixed) | 10 (fixed) | 10 (fixed) | 10 (fixed) | 10 (fixed) | 10 (fixed) | 10 (fixed) |
| | τ_2 | $0.14^{+0.05}_{-0.07}$ | ≤ 0.01 | ≤ 0.01 | ≤ 0.01 | ≤ 0.01 | $0.14^{+0.09}_{-0.06}$ | $0.14^{+0.08}_{-0.09}$ | ≤ 0.01 | $0.61^{+0.04}_{-0.05}$ | $0.57^{+0.05}_{-0.05}$ |
| Gaussian | E_{Fe} (keV) | 6.6 (fixed) | 6.6 (fixed) | 6.6 (fixed) | 6.6 (fixed) | 6.6 (fixed) | 6.6 (fixed) | 6.6 (fixed) | 6.6 (fixed) | 6.6 (fixed) | 6.6 (fixed) |
| | σ_{Fe} (keV) | 0.3 (fixed) | 0.3 (fixed) | 0.3 (fixed) | 0.3 (fixed) | 0.3 (fixed) | 0.3 (fixed) | 0.3 (fixed) | 0.3 (fixed) | 0.3 (fixed) | 0.3 (fixed) |
| | norm | $0.062^{+0.004}_{-0.007}$ | $0.057^{+0.003}_{-0.003}$ | $0.056^{+0.007}_{-0.004}$ | $0.048^{+0.007}_{-0.006}$ | $0.038^{+0.005}_{-0.006}$ | $0.041^{+0.006}_{-0.005}$ | $0.041^{+0.003}_{-0.008}$ | $0.043^{+0.005}_{-0.004}$ | $0.049^{+0.007}_{-0.005}$ | $0.052^{+0.007}_{-0.003}$ |
| bbodyrad1 | kT (keV) | $0.51^{+0.01}_{-0.01}$ | $0.50^{+0.01}_{-0.02}$ | $0.48^{+0.02}_{-0.02}$ | $0.44^{+0.02}_{-0.02}$ | $0.50^{+0.01}_{-0.03}$ | $0.50^{+0.01}_{-0.02}$ | $0.54^{+0.01}_{-0.02}$ | $0.58^{+0.01}_{-0.01}$ | $0.54^{+0.01}_{-0.01}$ | $0.55^{+0.02}_{-0.01}$ |
| | norm | 6438^{+649}_{-523} | 6460^{+753}_{-418} | 6672^{+839}_{-663} | 5825^{+885}_{-938} | 4196^{+1059}_{-269} | 5443^{+605}_{-553} | 5393^{+551}_{-375} | 5227^{+304}_{-228} | 5284^{+569}_{-352} | 5661^{+430}_{-418} |
| bbodyrad2 | kT (keV) | $1.70^{+0.02}_{-0.03}$ | $1.32^{+0.03}_{-0.07}$ | $1.48^{+0.06}_{-0.09}$ | $1.46^{+0.03}_{-0.06}$ | $1.51^{+0.06}_{-0.06}$ | $1.79^{+0.04}_{-0.08}$ | $1.54^{+0.05}_{-0.06}$ | $2.03^{+0.03}_{-0.03}$ | $1.69^{+0.04}_{-0.05}$ | $1.82^{+0.03}_{-0.02}$ |
| | norm | 262^{+13}_{-9} | 387^{+63}_{-33} | 128^{+16}_{-12} | 198^{+15}_{-10} | 160^{+20}_{-12} | 91^{+10}_{-7} | 189^{+24}_{-17} | 148^{+5}_{-6} | 153^{+12}_{-11} | 186^{+10}_{-11} |
| cutoffPL | Γ | $-0.88^{+0.02}_{-0.04}$ | $-0.41^{+0.03}_{-0.02}$ | $-0.26^{+0.03}_{-0.02}$ | $-0.24^{+0.03}_{-0.01}$ | $-0.37^{+0.03}_{-0.02}$ | $-0.54^{+0.04}_{-0.03}$ | $-0.72^{+0.03}_{-0.03}$ | $-0.98^{+0.04}_{-0.02}$ | $-0.12^{+0.03}_{-0.03}$ | $-0.44^{+0.03}_{-0.03}$ |
| | E_{fold} | $9.8^{+0.1}_{-0.1}$ | $10.5^{+0.1}_{-0.1}$ | $10.5^{+0.1}_{-0.1}$ | $10.5^{+0.1}_{-0.1}$ | $10.3^{+0.1}_{-0.1}$ | $9.8^{+0.1}_{-0.1}$ | $9.4^{+0.1}_{-0.1}$ | $9.2^{+0.1}_{-0.1}$ | $12.1^{+0.1}_{-0.1}$ | $11.0^{+0.1}_{-0.1}$ |
| | norm | $0.11^{+0.01}_{-0.01}$ | $0.44^{+0.04}_{-0.02}$ | $0.62^{+0.04}_{-0.03}$ | $0.62^{+0.04}_{-0.02}$ | $0.42^{+0.03}_{-0.02}$ | $0.31^{+0.03}_{-0.02}$ | $0.21^{+0.01}_{-0.01}$ | $0.09^{+0.01}_{-0.01}$ | $0.58^{+0.04}_{-0.04}$ | $0.28^{+0.02}_{-0.02}$ |
| Fitting | $\chi^2_{\text{red}}/\text{d.o.f}$ | 1.21/305 | 1.02/305 | 1.17/305 | 0.99/305 | 1.01/305 | 0.76/305 | 0.87/305 | 0.91/305 | 0.83/305 | 1.09/305 |

Note. Uncertainties are reported at the 90% confidence interval and were computed using MCMC of length 10,000. The 0.5%, 0.5%, and 1% system errors for LE, ME, and HE have been added during spectral fittings.

Table 2
Parameters of the Spectral Fitting

| Phase | | 0.0–0.1 | 0.1–0.2 | 0.2–0.3 | 0.3–0.4 | 0.4–0.5 | 0.5–0.6 | 0.6–0.7 | 0.7–0.8 | 0.8–0.9 | 0.9–1.0 |
|-----------|--|---------------------------|---------------------------|---------------------------|---------------------------|---------------------------|---------------------------|---------------------------|---------------------------|---------------------------|---------------------------|
| TBabs | n_{H} (10^{22} cm^{-2}) | 0.59 (fixed) | 0.59 (fixed) | 0.59 (fixed) | 0.59 (fixed) | 0.59 (fixed) | 0.59 (fixed) | 0.59 (fixed) | 0.59 (fixed) | 0.59 (fixed) | 0.59 (fixed) |
| mgabs | E_{cyc1} (keV) | $44.3^{+1.4}_{-1.2}$ | $44.5^{+1.3}_{-0.7}$ | $47.3^{+1.0}_{-0.8}$ | $47.1^{+0.8}_{-0.6}$ | $44.1^{+0.7}_{-0.4}$ | $44.5^{+1.0}_{-0.1}$ | $44.6^{+1.2}_{-0.9}$ | $45.3^{+1.4}_{-1.0}$ | $36.0^{+1.1}_{-0.9}$ | $38.5^{+1.9}_{-1.5}$ |
| | σ_1 (keV) | 12^{+4}_{-1} | 12^{+3}_{-2} | 12^{+2}_{-2} | 12^{+3}_{-1} | 12^{+2}_{-1} | 11^{+3}_{-1} | 11^{+3}_{-1} | 10^{+2}_{-1} | 11^{+3}_{-1} | 5^{+4}_{-1} |
| | τ_1 | $0.14^{+0.02}_{-0.01}$ | $0.19^{+0.02}_{-0.01}$ | $0.22^{+0.01}_{-0.01}$ | $0.22^{+0.02}_{-0.01}$ | $0.18^{+0.02}_{-0.01}$ | $0.15^{+0.03}_{-0.01}$ | $0.17^{+0.01}_{-0.01}$ | $0.17^{+0.01}_{-0.01}$ | $0.11^{+0.02}_{-0.01}$ | $0.05^{+0.01}_{-0.02}$ |
| | E_{cyc2} (keV) | 99^{+4}_{-3} | 103^{+7}_{-4} | 110^{+1}_{-10} | 99^{+5}_{-5} | 96^{+5}_{-2} | 93^{+12}_{-2} | 96^{+8}_{-2} | 93^{+6}_{-2} | 102^{+5}_{-2} | 100^{+2}_{-1} |
| | σ_2 (keV) | 6^{+5}_{-3} | 6^{+4}_{-1} | 5^{+8}_{-2} | 5^{+12}_{-1} | 5^{+5}_{-1} | 6^{+12}_{-1} | 6^{+7}_{-1} | 5^{+10}_{-1} | 12^{+5}_{-1} | 9^{+2}_{-1} |
| | τ_2 | $0.4^{+0.1}_{-0.1}$ | $0.3^{+0.1}_{-0.1}$ | $0.2^{+0.2}_{-0.1}$ | $0.1^{+0.1}_{-0.1}$ | $0.3^{+0.1}_{-0.1}$ | $0.2^{+0.1}_{-0.1}$ | $0.2^{+0.1}_{-0.1}$ | $0.2^{+0.1}_{-0.1}$ | $0.6^{+0.1}_{-0.1}$ | $0.6^{+0.1}_{-0.1}$ |
| Gaussian | E_{Fe} (keV) | 6.6 (fixed) | 6.6 (fixed) | 6.6 (fixed) | 6.6 (fixed) | 6.6 (fixed) | 6.6 (fixed) | 6.6 (fixed) | 6.6 (fixed) | 6.6 (fixed) | 6.6 (fixed) |
| | σ_{Fe} (keV) | 0.3 (fixed) | 0.3 (fixed) | 0.3 (fixed) | 0.3 (fixed) | 0.3 (fixed) | 0.3 (fixed) | 0.3 (fixed) | 0.3 (fixed) | 0.3 (fixed) | 0.3 (fixed) |
| | norm | $0.064^{+0.005}_{-0.005}$ | $0.056^{+0.006}_{-0.005}$ | $0.057^{+0.008}_{-0.003}$ | $0.049^{+0.006}_{-0.006}$ | $0.039^{+0.007}_{-0.003}$ | $0.043^{+0.007}_{-0.005}$ | $0.044^{+0.006}_{-0.004}$ | $0.043^{+0.006}_{-0.004}$ | $0.047^{+0.006}_{-0.008}$ | $0.050^{+0.003}_{-0.004}$ |
| bbodyrad1 | kT (keV) | $0.50^{+0.01}_{-0.01}$ | $0.51^{+0.01}_{-0.02}$ | $0.48^{+0.02}_{-0.01}$ | $0.44^{+0.02}_{-0.01}$ | $0.50^{+0.02}_{-0.02}$ | $0.49^{+0.01}_{-0.02}$ | $0.53^{+0.02}_{-0.02}$ | $0.58^{+0.01}_{-0.01}$ | $0.55^{+0.01}_{-0.02}$ | $0.56^{+0.01}_{-0.01}$ |
| | norm | 6588^{+423}_{-539} | 6270^{+661}_{-592} | 6821^{+740}_{-675} | 6115^{+881}_{-779} | 4319^{+647}_{-348} | 5541^{+1035}_{-363} | 5640^{+485}_{-486} | 5253^{+214}_{-327} | 5274^{+642}_{-424} | 5475^{+386}_{-293} |
| bbodyrad2 | kT (keV) | $1.65^{+0.03}_{-0.02}$ | $1.35^{+0.02}_{-0.06}$ | $1.37^{+0.09}_{-0.10}$ | $1.41^{+0.06}_{-0.05}$ | $1.47^{+0.06}_{-0.08}$ | $1.71^{+0.01}_{-0.08}$ | $1.44^{+0.05}_{-0.07}$ | $2.00^{+0.02}_{-0.02}$ | $1.75^{+0.03}_{-0.07}$ | $1.90^{+0.03}_{-0.02}$ |
| | norm | 277^{+10}_{-9} | 372^{+70}_{-16} | 152^{+11}_{-24} | 224^{+18}_{-15} | 175^{+27}_{-13} | 95^{+14}_{-3} | 222^{+36}_{-27} | 144^{+4}_{-7} | 152^{+20}_{-10} | 170^{+7}_{-5} |
| cutoffPL | Γ | $-0.85^{+0.03}_{-0.04}$ | $-0.45^{+0.01}_{-0.03}$ | $-0.26^{+0.02}_{-0.03}$ | $-0.27^{+0.02}_{-0.03}$ | $-0.38^{+0.02}_{-0.04}$ | $-0.53^{+0.03}_{-0.03}$ | $-0.70^{+0.02}_{-0.03}$ | $-0.89^{+0.03}_{-0.03}$ | $-0.17^{+0.03}_{-0.02}$ | $-0.42^{+0.03}_{-0.04}$ |
| | E_{fold} | $9.9^{+0.1}_{-0.1}$ | $10.3^{+0.1}_{-0.1}$ | $10.6^{+0.1}_{-0.1}$ | $10.4^{+0.1}_{-0.1}$ | $10.2^{+0.1}_{-0.1}$ | $9.8^{+0.1}_{-0.1}$ | $9.4^{+0.1}_{-0.1}$ | $9.4^{+0.1}_{-0.1}$ | $11.9^{+0.2}_{-0.1}$ | $11.1^{+0.1}_{-0.1}$ |
| | norm | $0.13^{+0.01}_{-0.01}$ | $0.41^{+0.01}_{-0.02}$ | $0.63^{+0.04}_{-0.02}$ | $0.60^{+0.02}_{-0.04}$ | $0.42^{+0.03}_{-0.03}$ | $0.32^{+0.02}_{-0.02}$ | $0.22^{+0.01}_{-0.02}$ | $0.11^{+0.01}_{-0.01}$ | $0.51^{+0.03}_{-0.02}$ | $0.28^{+0.02}_{-0.02}$ |
| Fitting | $\chi^2_{\text{red}}/\text{d.o.f}$ | 1.22/302 | 0.88/302 | 1.14/302 | 1.00/302 | 0.95/302 | 0.77/302 | 0.83/302 | 0.85/302 | 0.82/302 | 1.00/302 |

Note. Uncertainties are reported at the 90% confidence interval and were computed using MCMC of length 10,000. The 0.5%, 0.5%, and 1% system errors for LE, ME, and HE have been added during spectral fittings.

Table 3
Parameters of the Spectral Fitting

| Phase | | 0.0 – 0.1 | 0.1 – 0.2 | 0.2 – 0.3 | 0.3 – 0.4 | 0.4 – 0.5 | 0.5 – 0.6 | 0.6 – 0.7 | 0.7 – 0.8 | 0.8 – 0.9 | 0.9 – 1.0 |
|-----------|--|---------------------------|---------------------------|---------------------------|---------------------------|---------------------------|---------------------------|---------------------------|---------------------------|---------------------------|---------------------------|
| TBabs | n_{H} (10^{22} cm^{-2}) | 0.59 (fixed) | 0.59 (fixed) | 0.59 (fixed) | 0.59 (fixed) | 0.59 (fixed) | 0.59 (fixed) | 0.59 (fixed) | 0.59 (fixed) | 0.59 (fixed) | 0.59 (fixed) |
| gabs1 | E_{cyc1} (keV) | $43.6^{+1.4}_{-0.9}$ | $44.6^{+0.7}_{-0.5}$ | $47.1^{+0.6}_{-0.4}$ | $46.8^{+0.4}_{-1.1}$ | $44.0^{+0.9}_{-0.9}$ | $44.6^{+1.8}_{-0.9}$ | $44.3^{+1.2}_{-0.8}$ | $45.2^{+1.5}_{-0.8}$ | $36.7^{+2.1}_{-1.4}$ | $35.1^{+2.7}_{-1.4}$ |
| | σ_1 (keV) | 12^{+4}_{-1} | 11^{+2}_{-1} | 12^{+3}_{-2} | 12^{+3}_{-1} | 11^{+2}_{-1} | 10^{+2}_{-1} | 11^{+2}_{-1} | 10^{+2}_{-1} | 10^{+2}_{-1} | 2^{+2}_{-1} |
| | Strength1 | $4.7^{+1.4}_{-0.5}$ | $5.3^{+1.4}_{-0.1}$ | $7.5^{+1.4}_{-0.1}$ | $7.5^{+1.1}_{-0.2}$ | $5.5^{+0.4}_{-0.3}$ | $3.8^{+1.1}_{-0.5}$ | $5.4^{+1.0}_{-0.6}$ | $4.5^{+1.1}_{-0.7}$ | $2.3^{+1.1}_{-0.6}$ | $0.4^{+0.2}_{-0.1}$ |
| gabs2 | E_{cyc2} (keV) | 98^{+6}_{-3} | 103^{+10}_{-6} | ... | ... | 94^{+7}_{-3} | 93^{+6}_{-4} | 92^{+2}_{-2} | 93^{+12}_{-3} | 105^{+6}_{-3} | 101^{+3}_{-2} |
| | σ_2 (keV) | 5^{+4}_{-3} | 6^{+7}_{-4} | ... | ... | 4^{+7}_{-2} | 5^{+7}_{-4} | 1^{+1}_{-1} | 4^{+8}_{-3} | 13^{+7}_{-1} | 10^{+2}_{-1} |
| | Strength2 | 7^{+3}_{-2} | 5^{+8}_{-2} | ... | ... | $4^{+2}_{-1.0}$ | 4^{+3}_{-1} | 3^{+2}_{-2} | 3^{+4}_{-1} | 31^{+13}_{-7} | 22^{+5}_{-3} |
| Gaussian | E_{Fe} (keV) | 6.6 (fixed) | 6.6 (fixed) | 6.6 (fixed) | 6.6 (fixed) | 6.6 (fixed) | 6.6 (fixed) | 6.6 (fixed) | 6.6 (fixed) | 6.6 (fixed) | 6.6 (fixed) |
| | σ_{Fe} (keV) | 0.3 (fixed) | 0.3 (fixed) | 0.3 (fixed) | 0.3 (fixed) | 0.3 (fixed) | 0.3 (fixed) | 0.3 (fixed) | 0.3 (fixed) | 0.3 (fixed) | 0.3 (fixed) |
| | norm | $0.064^{+0.004}_{-0.006}$ | $0.058^{+0.003}_{-0.007}$ | $0.057^{+0.006}_{-0.007}$ | $0.050^{+0.007}_{-0.006}$ | $0.040^{+0.005}_{-0.003}$ | $0.044^{+0.006}_{-0.006}$ | $0.043^{+0.006}_{-0.005}$ | $0.043^{+0.006}_{-0.007}$ | $0.049^{+0.006}_{-0.004}$ | $0.052^{+0.005}_{-0.006}$ |
| bbodyrad1 | kT (keV) | $0.50^{+0.01}_{-0.02}$ | $0.49^{+0.01}_{-0.02}$ | $0.48^{+0.02}_{-0.01}$ | $0.44^{+0.02}_{-0.01}$ | $0.49^{+0.02}_{-0.02}$ | $0.48^{+0.01}_{-0.01}$ | $0.54^{+0.02}_{-0.02}$ | $0.58^{+0.01}_{-0.01}$ | $0.54^{+0.02}_{-0.01}$ | $0.55^{+0.01}_{-0.02}$ |
| | norm | 6706^{+722}_{-584} | 6728^{+921}_{-462} | 6996^{+882}_{-601} | 6305^{+1149}_{-791} | 4532^{+379}_{-735} | 5771^{+553}_{-403} | 5594^{+741}_{-610} | 5243^{+258}_{-338} | 5058^{+432}_{-462} | 5555^{+620}_{-404} |
| bbodyrad2 | kT (keV) | $1.64^{+0.03}_{-0.03}$ | $1.26^{+0.04}_{-0.03}$ | $1.39^{+0.09}_{-0.04}$ | $1.41^{+0.06}_{-0.01}$ | $1.43^{+0.06}_{-0.06}$ | $1.61^{+0.10}_{-0.07}$ | $1.48^{+0.03}_{-0.06}$ | $2.01^{+0.04}_{-0.02}$ | $1.71^{+0.05}_{-0.08}$ | $1.84^{+0.03}_{-0.03}$ |
| | norm | 284^{+19}_{-13} | 428^{+50}_{-25} | 162^{+23}_{-20} | 232^{+19}_{-9} | 189^{+30}_{-17} | 94^{+11}_{-8} | 217^{+34}_{-12} | 144^{+4}_{-7} | 132^{+12}_{-17} | 163^{+12}_{-7} |
| cutoffPL | Γ | $-0.89^{+0.02}_{-0.04}$ | $-0.39^{+0.01}_{-0.04}$ | $-0.29^{+0.01}_{-0.04}$ | $-0.28^{+0.01}_{-0.06}$ | $-0.38^{+0.02}_{-0.03}$ | $-0.48^{+0.03}_{-0.03}$ | $-0.75^{+0.03}_{-0.03}$ | $-0.90^{+0.04}_{-0.03}$ | $-0.05^{+0.03}_{-0.03}$ | $-0.31^{+0.03}_{-0.03}$ |
| | E_{fold} | $9.8^{+0.1}_{-0.1}$ | $10.5^{+0.1}_{-0.1}$ | $10.5^{+0.1}_{-0.1}$ | $10.4^{+0.1}_{-0.2}$ | $10.2^{+0.1}_{-0.1}$ | $9.9^{+0.1}_{-0.1}$ | $9.3^{+0.1}_{-0.1}$ | $9.4^{+0.1}_{-0.1}$ | $12.5^{+0.2}_{-0.2}$ | $11.4^{+0.1}_{-0.1}$ |
| | norm | $0.12^{+0.01}_{-0.01}$ | $0.47^{+0.01}_{-0.04}$ | $0.59^{+0.01}_{-0.01}$ | $0.58^{+0.01}_{-0.07}$ | $0.43^{+0.02}_{-0.03}$ | $0.37^{+0.02}_{-0.03}$ | $0.20^{+0.01}_{-0.01}$ | $0.10^{+0.01}_{-0.01}$ | $0.68^{+0.06}_{-0.05}$ | $0.36^{+0.02}_{-0.03}$ |
| Fitting | $\chi^2_{\text{red}}/\text{d.o.f}$ | 1.20/305 | 0.95/305 | 1.08/308 | 0.97/308 | 0.94/305 | 0.79/305 | 0.81/305 | 0.85/305 | 0.80/305 | 0.99/305 |

Note. Uncertainties are reported at the 90% confidence interval and were computed using MCMC of length 10,000. The 0.5%, 0.5%, and 1% system errors for LE, ME, and HE have been added during spectral fittings.

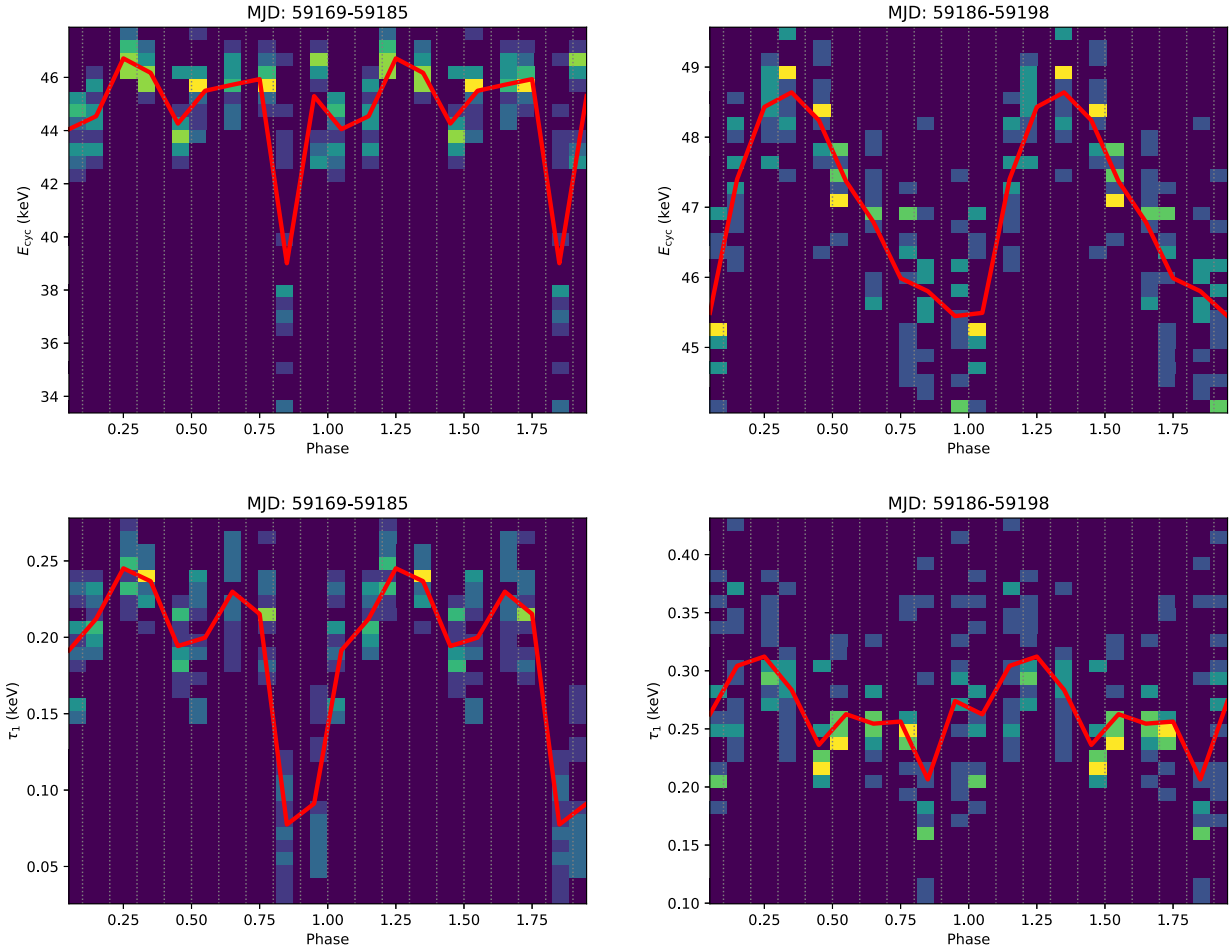


Figure 4. The left and right panels show the 2D histogram of E_{cyc} (top) and τ_1 (bottom) for luminosities above (MJD 59169 – 59185) and below (MJD 59186 – 59198) the critical luminosity. The red lines describe the average value of each phase. From the red lines of E_{cyc} , we found a significant transition from a single peak (subcritical area) into a double peak (supercritical area).

right panel of Figure 4. They convert to a double-peak shape between MJD 59169 and 59185 during the supercritical regime, and the line remained at ~ 45 keV with the exception of a reduction to ~ 40 keV at phases 0.8–0.9 as shown in the top left panel of Figure 4. The CRSF energies between phases 0.0 and 0.8 are higher than those between 0.8 and 0.9, with a modulation essentially near ~ 45 keV except a drop to ~ 40 keV. From the bottom panels of Figure 4, the absorption depth τ_1 keeps a double-peak shape within the whole outburst, while in Figure 3, the τ_2 shows significant absorption at phases 0.8–1.0 between MJD 59169 and 59185. We find that the absorption depths of τ_1 and τ_2 are inversely correlated at phase 0.8–1.0 (see Figure 5). The harmonic line is only visible in a narrow phase of 0.8–1.0, where the absorption depth of fundamental lines becomes weaker ($\tau_1 \leq 0.1$) and $E_{\text{cyc}} \leq 40$ keV between MJD 59169 and 59180.

Second, a transition of the nonthermal component from a broad single peak to double peaks, accompanied by a narrow ridge in phases 0.8–1.0, happens when luminosity exceeds L_{crit} . This change is reflected in Figure 3 through the evolution of parameters of the photon index Γ and cutoff energy E_{cut} .

4. Discussion

Based on Insight-HXMT’s high cadence and high statistic observations that covered the the entire giant (type II) outburst

of 1A 0535+262 in 2020, we have performed the detailed phase-resolved spectral analysis on both the CRSF and continuum spectral components and investigated their evolution throughout the outburst that covers a luminosity range of 7×10^{36} erg s $^{-1}$ to 1.2×10^{38} erg s $^{-1}$. In Kong et al. (2021), a significant anticorrelation between the fundamental CRSF energy and luminosities was found for the first time in this source above 6.7×10^{37} erg s $^{-1}$ based on the phase-average analysis, which was associated with a transition from sub- to supercritical accretion regime. As shown in Figure 3, where the two regimes are indicated with the dashed lines, the two regimes are characterized by different intrinsic beam patterns of emerging radiation, and correspondingly, a strong transition of the observed spectrum can be expected. In V0332+53, Lutovinov et al. (2015) found that the spectral parameter modulations with phases show different behaviors under different pulse profiles (see Figure 2 in their paper). Still, they did not show the details of the evolution with time. The parameters of nonthermal components and CRSFs changing with the phases are correlated to the optical depth, electron temperature, magnetic field intensity, and cross section in the accretion column under different viewing angles. For 1A 0535+262, using the high-cadence observations and phase-resolved spectral analysis, we can investigate parameters modulated with phases in detail.

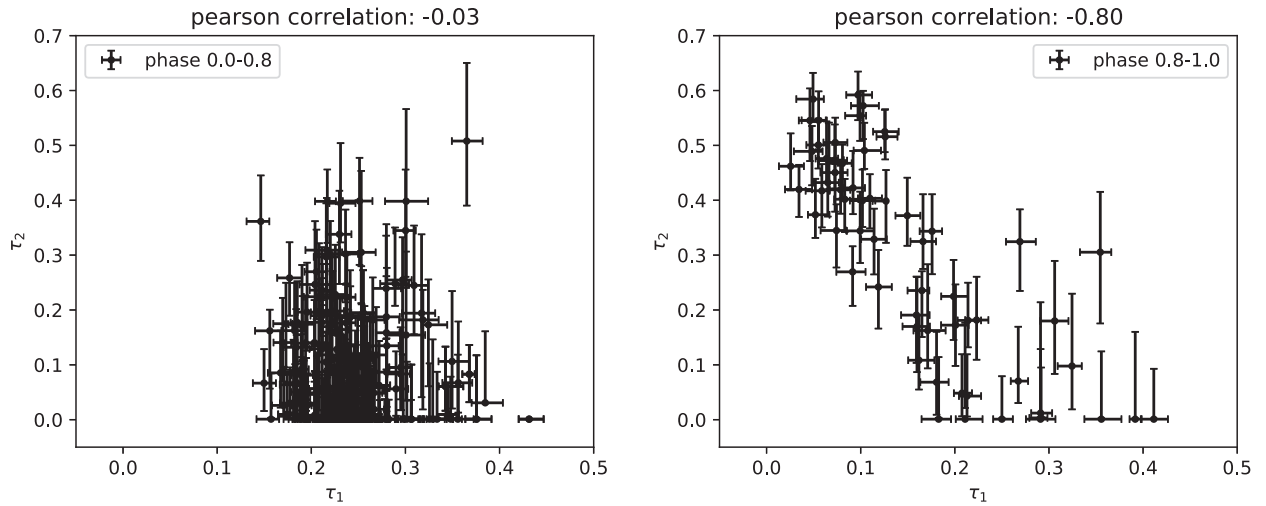


Figure 5. By showing the fitting results of absorption depth in all observations, there is no clear correlation in the left panel (Pearson correlation factor, $\rho = -0.03$) of τ_1 and τ_2 between phases 0.0 and 0.8, but a clear anticorrelation is shown in the right panel between phases 0.8 and 1.0 with large $\rho = -0.8$. Above the critical luminosity, most τ_2 between phases 0.0 and 0.8 is near zero.

In the left panel of Figure 1, the pulse profiles at luminosity $\sim 1.2 \times 10^{38} \text{ erg s}^{-1}$ (MJD 59171) are dominated by two peaks above 15 keV, which are generally attributed to the fan beam pattern above the critical luminosity (Davidson 1973). However, several peaks or dips underline the complexity of the pulse profile in the lower energy band. Section 3.1 noted that the two peaks' evolution with energy might be related to the relativistic beaming effect, especially the phase separation between the two peaks. Understanding this is difficult because of the radiation transfer complexity in the accretion column. For the beaming pattern, the higher the falling velocity, the more the radiation beam escapes from the column wall down to the NS surface rather than perpendicular to the magnetic field, which makes the phase separation of the two peaks of the fan beam move farther away. Thus, the assumption is that the falling material at the higher position of the accretion column has a larger velocity, leading to the high-energy radiation coming from the higher part of the column.

Above the critical luminosity, the parameters in different phases also show their complexity. In the right panel of Figure 1 and panels in Figure 3, the parameters of nonthermal component *cutoffpl* show double peaks, including a wide one and a narrow one. Interestingly, the narrow peak is only present at phases 0.8–1.0 when the outburst steps into the supercritical area between MJD 59169 and 59187. The smaller negative value of Γ implies a flatter spectrum, which in turn implies more high-energy photons, which is related to the increasing of pulse ratio in 50–70 keV and 70–90 keV. Meanwhile, at the same phase, the narrow peak below 15 keV might contribute to more soft photons and the softening of the continuum with larger Γ and the two blackbody components. Becker & Wolff (2005) used a bulk Comptonization process to describe the energy transition from the kinetic energy of falling matter to the radiation. In such “cold” plasma, the kinetic energy of electrons is far more than their thermal energy, which results in a power-law shape without an energy cut. This process may produce more high-energy photons, increasing E_{cut} .

For the CRSF line at the fundamental, the 2D distribution of line energy in Figure 3 splits into a double peak in phases 0.0–0.8, and the dip in phases 0.8–1.0 shows the shallowest absorption depth. The left and right panels of Figure 4 show the

2D histogram of fundamental CRSF parameters for luminosities above (MJD 59169–19185) and below (MJD 59186–19198) the critical luminosity. From the red lines in the two panels, we found a significant transition from a single peak (subcritical area) to a double peak (supercritical area). In phases 0.8–1.0, the first harmonic line becomes detectable with a depth greater than that of the fundamental. In Figure 5, we compare the correlation between τ_1 and τ_2 from all observations. Pearson correlation coefficient $\rho = -0.03$ for phases 0.0–0.8, and $\rho = -0.8$ for phases 0.8–1.0 denotes a strong anticorrelation for the latter line.

For 1A 0535+262, we can identify a relatively narrow range of phases and luminosities where parameters of the CRSF line and nonthermal continuum appear to exhibit rapid changes. Considering that the value of the corresponding luminosity at $\sim 6 \times 10^{37} \text{ erg s}^{-1}$ is consistent with the L_{crit} in Kong et al. (2021) and Mandal & Pal (2022), where the CRSF energy starts to show anticorrelation with luminosity, we surmise that the transition from sub- to supercritical accretion regime also responds to the transition in Figure 3. In Becker et al. (2012), the critical luminosity L_{crit} separates accretion column into two different patterns. When $L > L_{\text{crit}}$, the deceleration of matter in the sinking area below the radiation-dominated shock is dominated by radiation pressure, and hence the height of the column increases with luminosity. This results in the onset of a column with considerable height and optical depth along the magnetic field, and the radiation can only escape from the wall of the column, which is perpendicular to the magnetic field, forming the “fan beam” pattern that has been associated with double peaks of pulse profiles (Davidson 1973). We note that the height of the column can reach a few kilometers. Hence, high-energy photons that arise near the shock surface through bulk Comptonization (Becker & Wolff 2005) can be received effectively by the observer rather than be obscured or reflected by the NS (Poutanen et al. 2013), which might make it easier to see harmonics lines at higher energy during the supercritical regime. When $L < L_{\text{crit}}$, the height of the column decreases with luminosity, and flow might be stopped primarily by Coulomb collisions (Basko & Sunyaev 1976; Becker et al. 2012). In this subcritical regime, the top of the column is located nearer to the NS surface, where the plasma density is

very high. At the same time, the photons can mainly escape from the top along the magnetic field as a “pencil-beam” pattern (Burnard et al. 1991; Nelson et al. 1993).

Furthermore, through phase-resolved analysis by Insight-HXMT, we confirm the presence of the significant 100 keV line in 1A 0535+262 reported by Kendziorra et al. (1994), found only in a narrow phase range. We also note that a marginal detection (absorption depth unconstrained) of the possible third CRSF harmonic at ~ 128 keV was reported in the spectrum of MAXI J1409–619 (Orlandini et al. 2012). Here we give the highest significant detection of the highest energy of harmonic CRSF (see Caballero et al. 2007 for previous results). We note that similar behavior was reported by Klochkov et al. (2008) close to the maximum of the 2006 giant outburst in EXO 2030+375, and they also found a lower fundamental line depth when a prominent first harmonic line is present. We notice that the resonant scattering cross section at different resonance energies shows different behaviors (Harding & Daugherty 1991): for fundamental, $\sigma_{\text{res}}^1 \propto (1 + \cos^2 \theta)$, while for the first harmonic line, $\sigma_{\text{res}}^2 \propto (1 + \cos^2 \theta) \times \sin^2 \theta$. The θ is the angle between the photon momentum and the magnetic field. At different beaming patterns, the absorption depth for $n=1$ and $n=2$ is naturally different. In this interpretation, the “pencil beam” corresponds to $\sigma_{\text{res}}^2 \ll \sigma_{\text{res}}^1$. Thus, the harmonic line is naturally weak during the subcritical regime, which is consistent with our results in Figure 3. During the supercritical regime with “fan beam,” σ_{res}^2 and σ_{res}^1 can be comparable. Therefore, a deeper harmonic line absorption depth would be expected in this luminosity range. And we also notice that the harmonic absorption feature at higher energy sometimes makes the fundamental less deep than otherwise expected. During a strong absorption of the harmonic, the “photon spawn” effect and the “superposition” model have been suggested to account for a shallower fundamental line (Nishimura 2011, 2015). For the “photon spawn” effect, the fundamental absorption feature can be filled up when the electrons, which have been excited by a high-energy incident photon to a higher Landau level, decay and generate photons with the energy around the fundamental line (Schönherr et al. 2007). Nishimura (2011, 2015) focuses on the influence of a superposition of a large number of lines arising from different heights and argues that it is expected to dominate over photon spawning. Hence, a shallower fundamental line and a deeper harmonic line can be observed in the spectrum. However, these models tend to expect a gradual change of the CRSF energy with phases and thus might not be applicable for our observations of the harmonic lines (see the figures in Schönherr et al. 2007; Nishimura 2011, 2015).

We note that the pulse profiles have many complex components, which lead to another speculation. We speculate that the appearance of the first harmonic cyclotron line at a narrow phase during the supercritical phase might be associated with a peculiar line of sight concerning the reflection and eclipse of the emission by the NS surface. On one hand, the energy-dependent pulse profiles (left panel of Figure 1) with multipeak structure or multiple dips below 20 keV reveal complicated emission patterns originating from the eclipse by the NS surface (Klochkov et al. 2008; Mushtukov et al. 2018). On the other hand, the reflection of X-rays from the neutron surface that originated in the accretion column (Poutanen et al. 2013; Caballero et al. 2011) can contribute a considerable fraction of the emission that arises from a reflecting halo because a significant part of the radiation from the column wall

should be intercepted by the NS surface owing to relativistic beaming (Kaminker et al. 1976; Lyubarskii & Syunyaev 1988). The reflection model implies minor phase variations of the CRSF energy because it represents an average value of the magnetic field within a large area of the NS surface. This is consistent with our result of the fundamental line during the supercritical regime outside of the phase interval 0.8–1.0. However, when energy goes above 20 keV, the shape of the pulse profiles is generally more straightforward in double peaks, which implies that the high-energy photons from the higher part of the column cannot be affected by the NS surface in the direction of the line of sight. We also notice that the phase where the spectrum shows a strong absorption feature at 100 keV is not located at the peak of the pulse at high energy, which means that decreasing the numbers of high-energy photons by ellipse or reflection cannot explain the weak harmonic lines at other phases.

In Figure 1, the pulse profile in 20–40 keV is weakest in phases 0.8–1.0, which may be interpreted as the cap of the accretion column facing the observer under a fan beam pattern. Because of strong relativistic beaming toward the NS surface, the photons above 70 keV might come from the opposite accretion column at phases 0.8–1.0. And we resolve an additional component showing up in the pulse profile between the two peaks above 70 keV (see Figure 1, left panel). Therefore, there is another possibility that the two cyclotron lines come from different accretion columns. In the context of having a dipole magnetic field, the two accretion columns on the magnetic pole are symmetric and on opposite sides of the NS surface. Under this assumption, the high-energy photons generated at a specific height of the accretion column can create another emission pattern owing to the gravitational bending effect, while the accretion column is on the other side of the NS as an “anti-pencil”: the photons can be focused and become visible within a narrow phase (Sasaki et al. 2010; Mushtukov et al. 2018; Molkov et al. 2019). This new anti-pencil-beam pattern can contribute to high-energy photons subjected to cyclotron resonant scattering at 100 keV.










5. Conclusions

In this paper, the phase-resolved spectral analysis is used to explore the variation of spectral parameters with luminosity and phases. We discover the distribution and evolution of the parameters from CRSF and other spectral components below and above the critical luminosity. Above the critical luminosity, our results show that the absorption depth of the fundamental line is deeper in almost all periods, but it gets shallower and moves to lower energy at the appearance of the first harmonic, which can only be detected in a narrow phase interval. Here we surmise that the strict pulse phase dependence of the appearance of the harmonic line can be attributed to the “anti-pencil-beam” pattern. Future observation and theoretical modeling will investigate the probability of having such a pattern.

This work used data from the Insight-HXMT mission, a project funded by China National Space Administration (CNSA) and the Chinese Academy of Sciences (CAS). This work is supported by the National Key R&D Program of China (2021YFA0718500) and the National Natural Science Foundation of China under grants U1838201, U2038101, U1838202, 11733009, 12173103, U1838104, U1938101, U1938103, and

U2031205 and Guangdong Major Project of Basic and Applied Basic Research (grant No. 2019B030302001). M.O. acknowledges support by the Italian Space Agency under grant ASI-INAF No. 2017–14–H.O.

ORCID iDs

Ling-Da Kong  <https://orcid.org/0000-0003-3188-9079>
 Victor Doroshenko  <https://orcid.org/0000-0001-8162-1105>
 Andrea Santangelo  <https://orcid.org/0000-0003-4187-9560>
 Mauro Orlandini  <https://orcid.org/0000-0003-0946-3151>
 Filippo Frontera  <https://orcid.org/0000-0003-2284-571X>
 Jian Li  <https://orcid.org/0000-0003-1720-9727>
 Peng-Ju Wang  <https://orcid.org/0000-0002-6454-9540>
 Zhi Chang  <https://orcid.org/0000-0003-4856-2275>
 Shuang-Nan Zhang  <https://orcid.org/0000-0001-5586-1017>

References

- Arnaud, K. A. 1996, in ASP Conf. Ser., 101, *Astronomical Data Analysis Software and Systems V*, ed. G. H. Jacoby & J. Barnes (San Francisco, CA: ASP), 17
- Bailer-Jones, C. A. L., Rybizki, J., Fouesneau, M., Mantelet, G., & Andrae, R. 2018, *AJ*, 156, 58
- Basko, M. M., & Sunyaev, R. A. 1976, *MNRAS*, 175, 395
- Becker, P. A., Klochkov, D., Schönherr, G., et al. 2012, *A&A*, 544, A123
- Becker, P. A., & Wolff, M. T. 2005, *ApJ*, 630, 465
- Burnard, D. J., Arons, J., & Klein, R. I. 1991, *ApJ*, 367, 575
- Caballero, I., Kraus, U., Santangelo, A., Sasaki, M., & Kretschmar, P. 2011, *A&A*, 526, A131
- Caballero, I., Kretschmar, P., Santangelo, A., et al. 2007, *A&A*, 465, L21
- Caballero, I., Santangelo, A., Kretschmar, P., et al. 2008, *A&A*, 480, L17
- Canuto, V., & Ventura, J. 1977, *FCPh*, 2, 203
- Cao, X., Jiang, W., Meng, B., et al. 2020, *SCPMA*, 63, 249504
- Chen, Y., Cui, W., Li, W., et al. 2020, *SCPMA*, 63, 249505
- dal Fiume, D., Frontera, F., & Morelli, E. 1988, *ApJ*, 331, 313
- Davidson, K. 1973, *NPhS*, 246, 1
- Doroshenko, V., Tsygankov, S. S., Mushtukov, A. A., et al. 2017, *MNRAS*, 466, 2143
- Finger, M. H., Wilson, R. B., & Harmon, B. A. 1996, *ApJ*, 459, 288
- Grove, J. E., Strickman, M. S., Johnson, W. N., et al. 1995, *ApJL*, 438, L25
- Guo, C.-C., Liao, J.-Y., Zhang, S., et al. 2020, *JHEAp*, 27, 44
- Harding, A. K., & Daugherty, J. K. 1991, *ApJ*, 374, 687
- Harding, A. K., Meszaros, P., Kirk, J. G., & Galloway, D. J. 1984, *ApJ*, 278, 369
- Hobbs, G. B., Edwards, R. T., & Manchester, R. N. 2006, *MNRAS*, 369, 655
- Kaminker, A. D., Fedorenko, V. N., & Tsygan, A. I. 1976, *SvA*, 20, 436
- Kendziorra, E., Kretschmar, P., Pan, H. C., et al. 1994, *A&A*, 291, L31
- Klochkov, D., Santangelo, A., Staubert, R., & Ferrigno, C. 2008, *A&A*, 491, 833
- Klochkov, D., Staubert, R., Santangelo, A., Rothschild, R. E., & Ferrigno, C. 2011, *A&A*, 532, A126
- Kong, L. D., Zhang, S., Ji, L., et al. 2021, *ApJL*, 917, L38
- Kreykenbohm, I., Coburn, W., Wilms, J., et al. 2002, *A&A*, 395, 129
- Li, X., Li, X., Tan, Y., et al. 2020, *JHEAp*, 27, 64
- Liao, J.-Y., Zhang, S., Chen, Y., et al. 2020a, *JHEAp*, 27, 24
- Liao, J.-Y., Zhang, S., Lu, X.-F., et al. 2020b, *JHEAp*, 27, 14
- Liu, C., Zhang, Y., Li, X., et al. 2020, *SCPMA*, 63, 249503
- Lutovinov, A. A., Tsygankov, S. S., Suleimanov, V. F., et al. 2015, *MNRAS*, 448, 2175
- Lyubarskii, Y. E., & Syunyaev, R. A. 1988, *SvAL*, 14, 390
- Maitra, C. 2017, *JApA*, 38, 50
- Mandal, M., & Pal, S. 2022, *MNRAS*, 511, 1121
- Molkov, S., Lutovinov, A., Tsygankov, S., Mereminskiy, I., & Mushtukov, A. 2019, *ApJL*, 883, L11
- Mushtukov, A. A., Suleimanov, V. F., Tsygankov, S. S., & Poutanen, J. 2015, *MNRAS*, 447, 1847
- Mushtukov, A. A., Verhagen, P. A., Tsygankov, S. S., et al. 2018, *MNRAS*, 474, 5425
- Nelson, R. W., Salpeter, E. E., & Wasserman, I. 1993, *ApJ*, 418, 874
- Nishimura, O. 2011, *ApJ*, 730, 106
- Nishimura, O. 2015, *ApJ*, 807, 164
- Orlandini, M., Frontera, F., Masetti, N., Sguera, V., & Sidoli, L. 2012, *ApJ*, 748, 86
- Postnov, K., Staubert, R., Santangelo, A., et al. 2008, *A&A*, 480, L21
- Poutanen, J., Mushtukov, A. A., Suleimanov, V. F., et al. 2013, *ApJ*, 777, 115
- Rosenberg, F. D., Eyles, C. J., Skinner, G. K., & Willmore, A. P. 1975, *Natur*, 256, 628
- Sartore, N., Jourdain, E., & Roques, J. P. 2015, *ApJ*, 806, 193
- Sasaki, M., Klochkov, D., Kraus, U., Caballero, I., & Santangelo, A. 2010, *A&A*, 517, A8
- Schönherr, G., Wilms, J., Kretschmar, P., et al. 2007, *A&A*, 472, 353
- Staubert, R., Trümper, J., Kendziorra, E., et al. 2019, *A&A*, 622, A61
- Steele, I. A., Negueruela, I., Coe, M. J., & Roche, P. 1998, *MNRAS*, 297, L5
- Taylor, J. H. 1992, *RSPTA*, 341, 117
- Vybornov, V., Doroshenko, V., Staubert, R., & Santangelo, A. 2018, *A&A*, 610, A88
- Wilms, J., Allen, A., & McCray, R. 2000, *ApJ*, 542, 914
- Zhang, S., Lu, F. J., Zhang, S. N., & Li, T. P. 2014, *Proc. SPIE*, 9144, 914421
- Zhang, S.-N., Li, T., Lu, F., et al. 2020, *SCPMA*, 63, 249502